Nanoscale

PAPER

Cite this: *Nanoscale*, 2018, **10**, 1987

In situ tailoring of superconducting junctions *via* electro-annealing†

Joseph Lombardo, *[a] Željko L. Jelić,[a,b] Xavier D. A. Baumans,[a] Jeroen E. Scheerder, [c] Jorge P. Nacenta,[d] Victor V. Moshchalkov,[c] Joris Van de Vondel, [c] Roman B. G. Kramer,[d] Milorad V. Milošević[b] and Alejandro V. Silhanek[a]

Received 16th November 2017,
Accepted 28th December 2017

DOI: 10.1039/c7nr08571k

rsc.li/nanoscale

We demonstrate the *in situ* engineering of superconducting nanocircuitry by targeted modulation of material properties through high applied current densities. We show that the sequential repetition of such customized electro-annealing in a niobium (Nb) nanoconstriction can broadly tune the superconducting critical temperature T_c and the normal-state resistance R_n in the targeted area. Once a sizable R_n is reached, clear magneto-resistance oscillations are detected along with a Fraunhofer-like field dependence of the critical current, indicating the formation of a weak link but with further adjustable characteristics. Advanced Ginzburg–Landau simulations fully corroborate this picture, employing the detailed parametrization from the electrical characterization and high resolution electron microscope images of the region within the constriction where the material has undergone amorphization by electro-annealing.

1 Introduction

The Josephson effect[1] is arguably the utmost manifestation of macroscopic quantum coherence in superconductivity. Among the applications employing this phenomenon one finds (i) superconducting quantum interfometers, highly sensitive devices for detecting magnetic fields, suitable even for magnetoencephalography,[2] (ii) the most accurate voltage standard, with uncertainty of less than one part per billion,[3,4] (iii) a viable contender for reliable and scalable qubits,[5,6] and (iv) solutions for an exceedly performant nanothermometry.[7] The common denominator in all those devices is the need for advanced (controllable, tunable, and versatile) fabrication of weak link(s) between two superconducting banks, permitting the tunneling of superconducting Cooper pairs.

Over the past decades several methods for manufacturing small superconducting weak links have been developed, including tunnel barriers through a grain boundary,[8] over normal metal insertions,[9] depletion of the superconducting condensate with a ferromagnetic nanowire,[10] or promoting the formation of phase-slip lines.[11] In all cases, the properties of the weak link are preset by the fabrication protocol and once defined, they can no longer be modified. Tunable solutions to date are the electrostatic shrinkage of a junction by a gate voltage in ballistic junctions,[12] current-controllable planar S–(S/F)–S Josephson junctions,[13] and junctions controlled by localized external electric field in superconductor-ferroelectric coplanar structures.[14] While proven in practice, these solutions are rather involved and limited to specific materials, thus making it relevant both from academic and technological standpoint to identify alternative routes to create and controllably modify the properties of a superconducting junction.

In this work we identify controlled electro-annealing (EA) by high electric current densities as a viable method to produce weak links in superconducting nanostructures, with tunable characteristics in a broad range. It is well established that large applied electric current can alter the internal structure of a given material, *e.g.* change the grain structure,[15,16] or the Young's modulus,[17] cause athermal crystallization of the amorphous phase,[18,19] tune the stoichiometry of complex compounds,[20,21] or shrink down the lateral size of nanoconstrictions.[22] This can be achieved either by electropulsing, where a

[a]*Experimental Physics of Nanostructured Materials, Q-MAT, CESAM, Université de Liège, B-4000 Sart Tilman, Belgium. E-mail: j.lombardo@uliege.be; Tel: +32(0)43663630*
[b]*Departement Fysica, Universiteit Antwerpen, Groenenborgerlaan 171, B-2020 Antwerpen, Belgium*
[c]*Laboratory of Solid-State Physics and Magnetism, KU Leuven, Celestijnenlaan 200 D, box 2414, BE-3001 Leuven, Belgium*
[d]*Université Grenoble Alpes, CNRS, Grenoble INP, Institut Néel, 38000 Grenoble, France*

†Electronic supplementary information (ESI) available: High resolution SEM images show the polycrystalline structure of a virgin Nb nanoconstriction and the local amorphization of the same sample after several electro-annealing processes. Transport measurements showing the time-dependence of the sample resistance for several constant values of the bias current. See DOI: 10.1039/C7NR08571K

condenser is discharged within a decay time of few hundreds of μs, or by a feedback-controlled dc current able to induce continuous changes in the sample.[21]

Here we apply electro-annealing to locally change the superconducting properties of a Nb nanoconstriction, and thereby broadly tune the characteristics of the resulting junction. We chose a bow-tie geometry for the constriction, so that even a relatively small applied current can have significant effect due to its crowding (*i.e.* large density) at the narrowest point of the sample. By progressively increasing the applied current, we first identify a regime for current densities at the constriction below 100 MA cm^{-2}, where the superconducting properties of the constriction are slightly improved compared to the lateral banks. Within this regime the superconducting critical temperature (T_c) and critical current (I_c) increase, while the normal state resistance (R_n) decreases, thus transforming the system in a S–S′–S junction with $T_c(S') > T_c(S)$. When the maximum applied current (electro-annealing current) is increased above 100 MA cm^{-2}, a rapid deterioration of the superconducting properties takes place in the constriction, and the system switches to a S–S′–S junction with $T_c(S') < T_c(S)$. In other words, a weak link is formed. Under such circumstances, one expects the critical current to decline and eventually exhibit Fraunhofer-like oscillations as a function of the out-of-plane magnetic field (B). These oscillations can be regarded as a fingerprint of a superconducting weak link. In what follows, we demonstrate the experimental realization of such control performed *in situ*, as the first of its kind.

2 Results and discussion

2.1 Electro-annealing and sample characterization

We begin by analyzing the changes induced in the material by the electro-annealing process. The used transport bridges with a nanoconstriction were fabricated in a top-down process by etching a Nb film of 50 nm thickness, as elaborated in Methods. The top panels of Fig. 1 show scanning electron microscopy (SEM) images corresponding to (a) the virgin sample, (b) after weak electro-annealing with a maximum current $I_{EA} < 7.5$ mA, and (c) after strong electro-annealing with $I_{EA} > 7.5$ mA. These SEM images show that for applied currents above 7.5 mA, corresponding to current density of about 100 MA cm^{-2} at the constriction, the material properties strongly change in a region extending few hundred nanometers away from the isthmus of the bridge. Further electro-annealing led to a slight expansion of this region and eventually caused displacement of atoms, better known as electromigration, and the formation of a gap separating the two superconducting leads.[22]

After each EA process the $R(T)$ characteristics of the sample were systematically acquired so as to track the evolution of the conducting properties of the bridge. A selected set of $R(T)$ curves obtained with an applied current of 1 μA is shown in Fig. 1(d). Substantially lower feeding currents of 10 nA show no significant shift of the characteristics, demonstrating little-to-no heating effects in the samples.

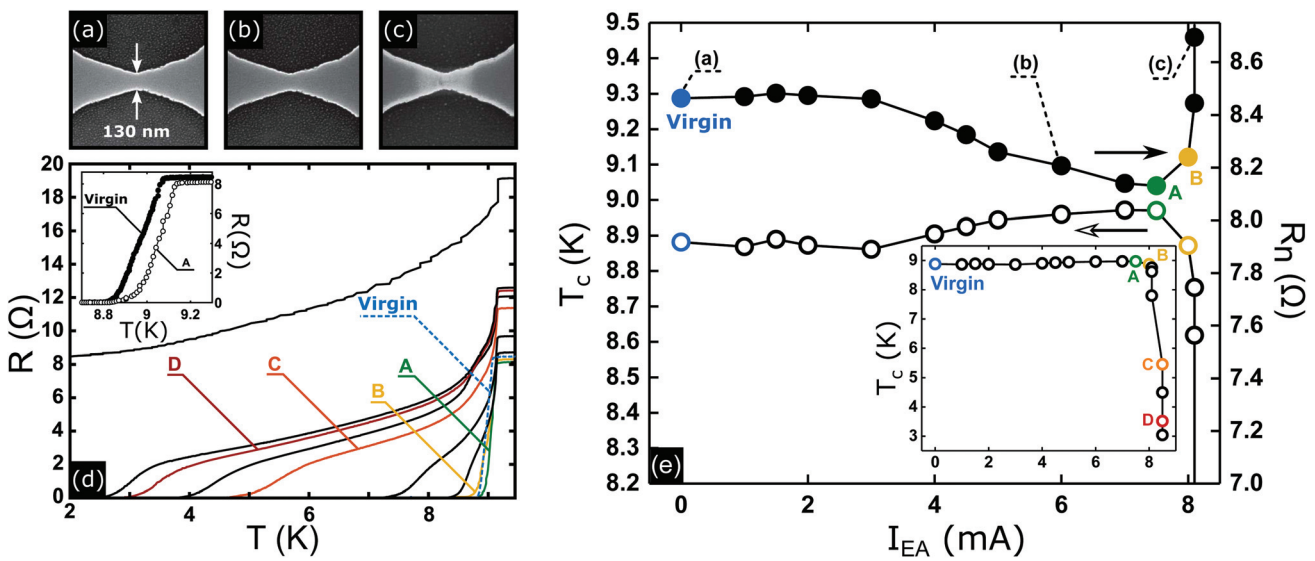

Fig. 1 Electro-annealing of Nb constrictions. (a) Scanning electron microscopy (SEM) image of a virgin Nb constriction. Panel (b) shows the same constriction as in (a) after the first EA process, leading to annealed material in the junction and decrease of the normal-state resistance, although without noticeable change in the SEM image. After multiple EA processes, the SEM image in (c) shows a central zone where the material properties have been deteriorated. (d) Measured $R(T)$ characteristics after subsequent EA processes. The inset shows the improvement of the conducting properties after the initial gentle EA, in the stage denoted as A. All subsequent stages of electro-annealing exhibit suppressed superconductivity (progressively larger normal-state resistance) in the constriction. Panel (e) shows the superconducting critical temperature of the constriction T_c (left ordinate) and the corresponding normal-state resistance R_n (right ordinate) as a function of the annealing current I_{EA}. The labels (a), (b), and (c) refer to the corresponding SEM images. The inset shows the evolution of the critical temperature at the center of the constriction for the whole range of explored I_{EA}. Different electro-annealing stages A, B, C, and D of the same device, are indicated.

Strikingly, the first effect of EA is to improve the conducting properties of the bridge. Indeed, for the low I_{EA} regime (I_{EA} < 7.5 mA), the normal-state resistance of the bridge decreases and the superconducting critical temperature in the constriction increases, as shown in the inset of Fig. 1(d). Note that within this regime no hint of material change is seen in the SEM images [Fig. 1(b)]. This enhancement of both the conducting and superconducting properties of the nanoconstriction could be ascribed to a current-induced recrystallization process similar to that reported by Aref and Bezryadin[19] in Mo_3Ge nanowires, or simply to a thermally-assisted degassing process[23] in view of the relatively high temperatures that can be reached at the constriction.[21]

The effects of the EA process are more clearly shown in Fig. 1(e), where the normal-state resistance R_n (right ordinate) and the superconducting critical temperature of the constriction T_c (left ordinate) are plotted as a function of the annealing current I_{EA}. Here one sees that for I_{EA} exceeding a threshold value of about 7.5 mA the nanoconstriction degrades very quickly, as evidenced by a sudden increase of the normal resistance accompanied by a decrease of T_c. This transition corresponds well with the SEM image in Fig. 1(c) evidencing a local change of the material properties. High-resolution SEM images (see ESI†) allow us to identify an amorphization of the material at the central region of the constriction as a source for the change. Since during electro-annealing a local temperature as high as 970 K can be reached at the constriction,[21] the amorphization may result from the combined effects of high temperature and oxygen diffusion in Nb which is known to become important above 400 K.[24] The presence of oxygen can be either due to the fact that the EA is not performed under ultra-high vacuum conditions or stem from the SiO_2 substrate (see Methods). One should remark that the observed current-induced changes in Nb, although highly controllable, are nearly irreversible.

All $R(T)$ characteristics for samples after EA with current I_{EA} > 7.5 mA, as shown in Fig. 1(d), evidence a two-step superconducting transition. As the temperature is lowered, the first resistance drop occurs at $T_c^{(0)}$ = 8.88 K regardless of the EA. This first resistance jump corresponds to the superconducting transition in part of the Nb sample near the voltage contacts that remains unaffected by the EA. This is followed by a second drop to zero resistance at lower temperatures. To extract the critical temperature for the superconducting-to-normal transition at the constriction, T_c, plotted in Fig. 1(e), we used an empirical 1 Ω criterion for the threshold resistance. The uppermost curve in Fig. 1(d) corresponds to the sample after applying a high current of 10 mA, able to displace atoms and change the overall geometry of the constriction. In Fig. 1, four different chronologically ordered electro-annealing stages A, B, C, and D of the same device, are indicated.

In an attempt to correlate the current-induced changes in resistivity of the constriction ρ_{WL} with the decrease of the superconducting critical temperature T_c in the constriction, we assume that (i) the spatial extent b of the affected material remains constant after each EA process, and (ii) the constriction has an idealized bow-tie geometry as sketched in the inset of Fig. 2. The former hypothesis is a zeroth-order approximation since the parameter b is likely determined by the extension of the hot spot centered at the constriction which in turn should progressively increase as I_{EA} increases. Nevertheless, this approximation is sufficient for the purpose of this paper, as will be shown further on.

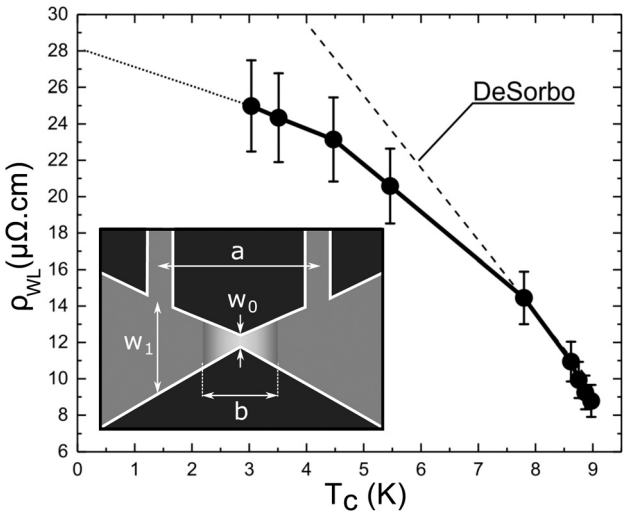

Fig. 2 Evolution of resistivity and superconducting critical temperature in the constriction. Main panel: Resistivity of the constriction as estimated using eqn (1), as a function of the measured superconducting critical temperature of the constriction. The error bars account for the uncertainty regarding the actual size of the electro-annealed region b. The dashed line corresponds to DeSorbo's prediction obtained for different concentrations of interstitial solute atoms of oxygen in Nb.[23] Inset: Sketch of the sample layout indicating the geometrical parameters at play in eqn (1).

Under these approximations, the total resistance of the sample is given by

$$R_N = \frac{a}{d(w_1 - w_0)}\left[\rho_{WL}\ \ln\ \left(1 + \frac{(w_1 - w_0)b}{w_0 a}\right) - \rho_0\ \ln\ \left(\frac{w_0}{w_1} + \frac{(w_1 - w_0)b}{w_0 a}\right)\right], \quad (1)$$

where geometric parameters a, b, w_0 and w_1 are indicated in the inset of Fig. 2, ρ_0 is the resistivity of the virgin Nb film (in our case ρ_0 = 10.0 ± 0.2 μΩ cm at 10 K), and d is the sample thickness. From this equation, we extract the resistivity of the weak link, ρ_{WL}, taking for remaining parameters a = 2000 nm, w_1 = 1100 nm, w_0 = 147 nm, b = 294 nm, and d = 50 nm. The obtained ρ_{WL} *versus* T_c correlation is shown in the main panel of Fig. 2. We suggested above that oxygen diffusion during EA could be boosted by the local high temperatures and lead to the observed decrease of T_c (increase of R_n). It is interesting to compare our data with that of Nb containing interstitial solute atoms of oxygen discussed in ref. 23, where it was found that for each 1 at% of O in pure Nb, the superconducting transition temperature decreases by 0.93 K and the normal-state resistivity increases by 5.2 μΩ cm. As shown in Fig. 2, this trend is repro-

duced by the low-resistivity data but fails to capture the high-resistivity data. A priori, this is somewhat expected since DeSorbo's rule only applies for oxygen concentrations below the solubility limit, which corresponds to a minimum T_c = 5.8 K. There are however further considerations which can be invoked to explain the observed difference. For one, we have assumed that b remains constant after subsequent EA processes, while b could be progressively increasing for I_{EA} > 7.5 mA. However by allowing b to be an adjustable parameter, we found that b should progressively decrease after each EA in order for our data to reproduce DeSorbo's linear trend. This is clearly unphysical, hence permits us to rule out the variation of b as a source of the observed discrepancy. In addition, DeSorbo only considered clean bulk Nb with RRR values much larger than the RRR ≈ 3 measured in our films. An additional (additive) effect is the possible contamination of the Nb by the silicon substrate to form Nb_5Si_3 during EA.[25]

In order to further characterize the samples after electro-annealing, we employ the established relation[26] for Nb $\rho\ell$ = 3.75×10^{-6} μΩ cm^2, to obtain the mean free path of the leads $\ell^{(0)}$ = 3.73 ± 0.08 nm. This allows us to calculate the superconducting coherence length at zero temperature $\xi(0)$ = 9.7 ± 0.3 nm, taking BCS ξ_0 = 39 nm for Nb, as well as to determine the progressively decreasing mean free path in the weak link (ℓ_{WL}) in samples A–D, according to the ρ_{WL} plotted in Fig. 2. With that information at hand, we resort to theoretical modeling of the transport properties of the samples, in order to gain further insights in the physical mechanism at play. For this purpose, we employ the time-dependent Ginzburg–Landau (TDGL) theory, which we adapted to account for spatially inhomogeneous parameters of the sample, as encountered in S–S′–S junctions of interest here. In this model, we introduced spatially-dependent variables T_c, ℓ and ρ as obtained from the experiment, and also modified the temperature dependencies of the relevant quantities.[27] As such, TDGL can provide more trustworthy results even for temperatures significantly below the critical temperature. The details of the model can be found in the Methods section. The specimen size, precise shape, bath temperature, and material parameters are taken from the experimental data obtained for the specimens C and D. The simulated sample geometry is directly taken from the high-resolution SEM images, corresponding to the part of the experimental sample between the voltage contacts, as shown in Fig. 1(a). Based on the available information for the weak-link area after final EA (SEM image shown in ESI†), the width of the weak link was fixed to b = 294 nm.

With this information, we calculated the $R(T)$ curves for samples C and D, presented in Fig. 3(a). Our first approach was based on the assumption that T_c^{WL}, ℓ_{WL}, and ρ_{WL}, obtained from the experiment, are uniform within the weak link as shown by their profiles along the sample depicted in the insets of Fig. 3. Although the overall behavior of the simulated $R(T)$ characteristics was quite satisfactory, the discrepancy from the experimental data was evident. Due to the lensing of currents inside the constriction, it is actually reasonable to assume that material modifications caused by the electro-annealing will not be uniform in the weak link. In absence of a better guess for ρ_{WL} and ℓ_{WL}, we introduced the spatial variation in the critical temperature of the form $T_c(r) = T_c^{(0)} - \Delta T_c \cdot e^{-(2|x|/b)^3}$, where x = 0 designates the center of the constriction and ΔT_c is the critical temperature difference between the leads ($T_c^{(0)}$) and the center of the weak link (T_c^{WL}). A contourplot of this spatially-varying critical temperature together with its profile along the entire sample is given as inset in Fig. 3(b). As

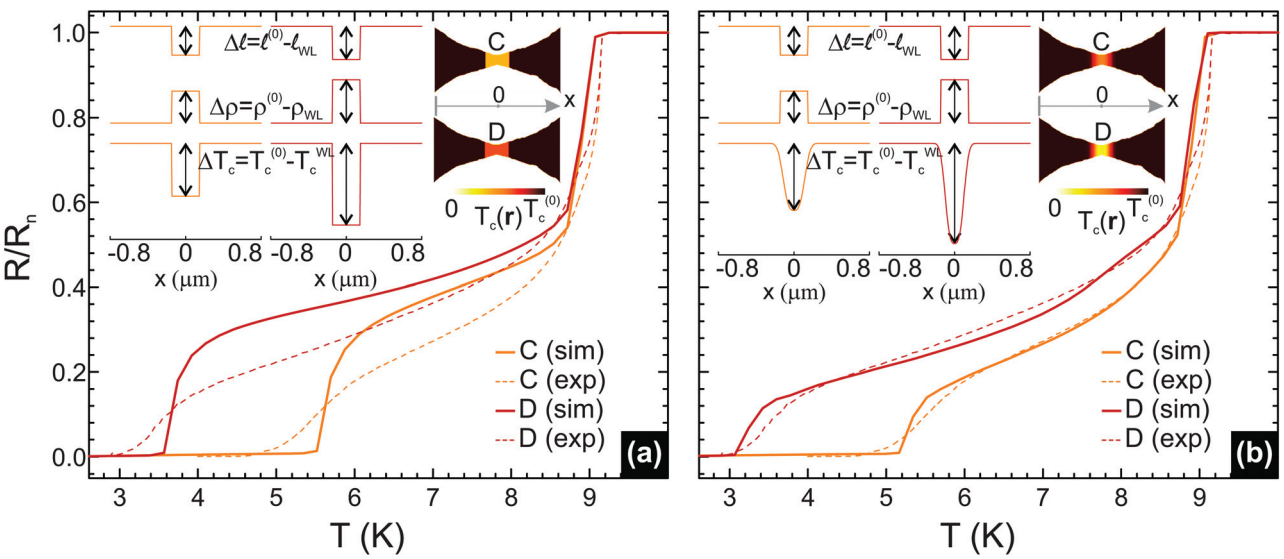

Fig. 3 Simulated $R(T)$ characteristics. (a) The results obtained using TDGL simulations for samples C (orange line) and D (red line), when all the parameters of the weak link are taken homogeneous, as depicted in the insets. (b) $R(T)$ curves simulated for samples C and D when the critical temperature was taken inhomogeneous in the weak link. Optimal distributions of $T_c(r)$ are shown in the inset for both samples. Corresponding experimental data is presented with dashed lines in both (a) and (b).

in the previous case, the rest of the material parameters are maintained constant. The results of the modified approach are presented in Fig. 3(b), where excellent agreement between experimental data (dashed lines) and simulations (solid lines) is apparent, using $\Delta T_c = 4.39$ K for sample C and $\Delta T_c = 6.06$ K for sample D.

2.2 Evidence of a tunable junction

The two-step transition in the $R(T)$ curves exhibits a resistance plateau between T_c^{WL} and $T_c^{(0)}$ (= 8.88 K). Within this temperature interval, the constriction is in the normal state, and there is no coherent superposition of the superconducting condensates of the leads. Therefore, the overall critical current of the junction is zero, being outside the diffusive limit of superconductor–normal metal–superconductor (SNS) junctions.[9,28,29] However, for temperatures $T < T_c^{WL}$ a weak link between the two superconducting leads develops and a supercurrent through the weak link can be established. As a consequence, the interplay of the Meissner current and the applied current can induce Fraunhofer-like behavior of the critical current, as schematically shown in Fig. 4 and described in detail in ref. 30 and 31.

Indeed, the Meissner current density J_M, induced as a response of the system to the external magnetic field, flows in opposite directions along the facing edges of the sample [panel 1 in Fig. 4(a)], and is superimposed to the density of the transport current (J_a) crowded in the constriction [panel 2 in Fig. 4(a)]. The total current density (J_T) is, therefore, enhanced on one edge of the sample ($J_T = J_a + J_M$), while being lowered on the opposite edge ($J_T = J_a - J_M$) [panel 3 in Fig. 4(a)].

This interplay of currents will affect the vortex entrance and exit barriers in the junction. A vortex enters the junction when at one side J_T reaches the depairing current density (J_{DP}). On the other side, if the applied current is large enough to fully deplete the Meissner current ($J_T \geq 0$), the exit barrier will vanish and the vortex can vacate the sample.[32] This defines the critical applied current $I_a = I_c$ for which the onset of the resistive state occurs due to periodic crossing of vortices along the junction.

With increasing magnetic field B, the Meissner currents in the sample become larger so that lower J_a is needed for a vortex to enter, thus yielding a decreasing $I_c(B)$. However, lowering J_a eventually recovers the barrier for vortex exit, so with further increasing B a larger applied current is needed to suppress the exit barrier for the vortex and I_c grows. At certain field, the conditions for the appearance of the new vortex and for vanishing exit barrier are met for the same I_a, and the onset of motion corresponds again to the condition $J_T = J_{DP}$, so that for larger field $I_c(B)$ decreases again. In this way, the oscillatory behavior of $I_c(B)$ is established, where every oscillation corresponds to one additional vortex traversing the junction. With every oscillation the amplitude of I_c decreases, as superconductivity is weakened by the magnetic field. All together, a typical Fraunhofer-like characteristic is obtained [Fig. 4(b)]. Although similar physics holds for the sample without a weak link, the oscillations in $I_c(B)$ are washed out in that case due to the fact that after penetrating at the constriction, vortices escape to the leads where the current density is lower. The suppression of superconductivity inside the weak link, as shown in panel 4 of Fig. 4(a), directly affects the Meissner currents and substantially lowers the critical conditions for vortex

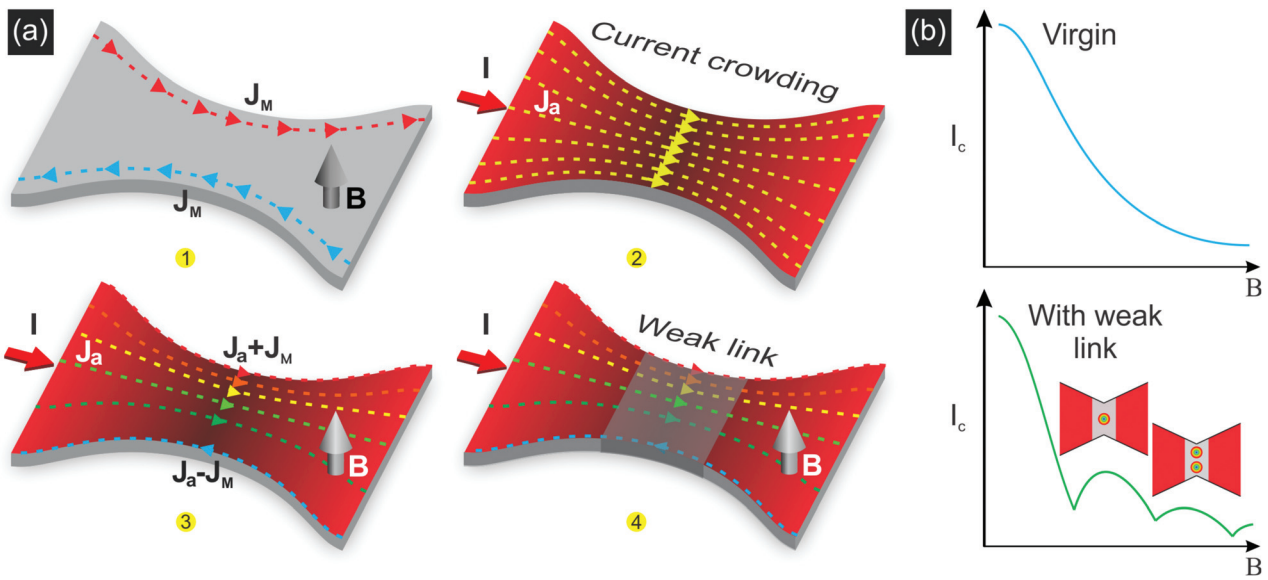

Fig. 4 The interplay of currents. Panels in (a) illustrate the behavior of the Meissner current J_M screening the applied magnetic field B ①, the distribution of the applied current crowded in the constriction ②, and the total current as the superposition of the previous two ③. Panel ④ schematically shows the region where the superconducting properties have been depleted by electro-annealing producing a weak link. The opposite behavior of the superimposed currents on the two facing edges of the constriction leads to Fraunhofer-like oscillations in $I_c(B)$ in the presence of a weak link, as shown in (b), and not in the virgin sample (without a weak link). Each oscillation corresponds to one additional vortex at the weak link.

entry/exit. In other words, the weak link acts as a mesoscopic sample inside the device dominating its $I_c(B)$ in both the amplitude and the period of the exhibited oscillations.

In order to prove the above described scenario in our samples and the tunability of $I_c(B)$, we have recorded $V(I)$ characteristics as a function of the applied magnetic field B perpendicular to the plane of the sample, and used a criterion of 10 μV to determine the critical current I_c of the constriction. A summary of the obtained $I_c(B)$ for a selected set of samples is shown in Fig. 5(a).

The virgin constriction exhibits a monotonic decrease of I_c as B increases. In the sample obtained after a weak EA process (curve A), where superconducting properties of the constriction were improved, the critical current of the junction increases by roughly 20% with respect to that of the virgin sample at the same temperature T = 8.5 K. This is in line with the estimated increase of both T_c and ℓ in the constriction, leading to approximately 30% increase of the depairing current density in the constriction $J_{DP} \propto \sqrt{\ell} T_c^{3/2} \left(1 - \frac{T^2}{T_c^2}\right) \sqrt{1 - \frac{T^4}{T_c^4}}$ (see Methods).

When the sample reaches the stage of EA indicated by A, the constriction can be regarded as a S–S′–S junction with $T_c(S') > T_c(S)$. Further EA (stage B) leads to suppression of

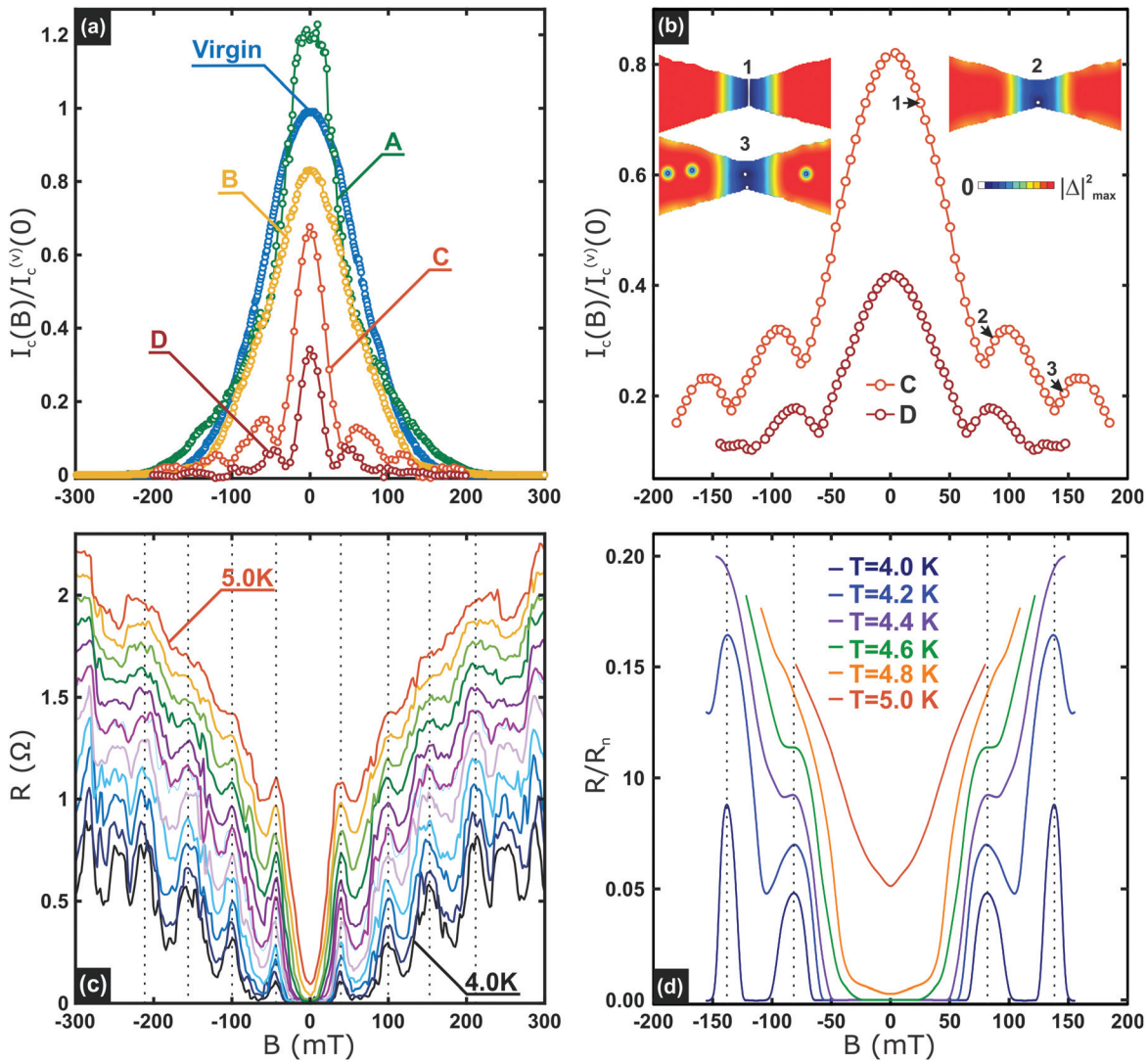

Fig. 5 Critical current and magnetoresistance oscillations. (a) Magnetic field dependence of the critical current $I_c(B)$ for a Nb nanoconstriction after different electro-annealing processes. All critical current values have been normalized by $I_c(B = 0)$ of the virgin sample. Chronologically, the original sample is labeled as virgin, then A, B, C, and D, respectively after subsequent electro-annealing processes. The reduced temperatures at which shown curves have been obtained are: T/T_c = 0.96 for virgin, A and B, T/T_c = 0.71 for C and D with T_c = 8.9 K. Panel (b) shows the simulated $I_c(B)$ characteristics for samples C and D, scaled with the critical current at zero field of the virgin sample. The insets show Cooper-pair density $|\Delta|^2$ snapshots corresponding to the onset of vortex dynamics at each oscillation of the $I_c(B)$ curve for this particular sample. Panels (c) and (d) show respectively the measured and the calculated magnetoresistance oscillations for the sample in state C, for temperatures between 4 K and 5 K.

superconductivity in the constriction, reflected in both lower $T_c(S')$ and lower ℓ_{WL}, with a corresponding decrease of $I_c(0)$ according to the expected decrease of J_{DP}. At the same time, $I_c(B)$ obtained at T = 8.5 K remains featureless. However, for sufficient suppression of $T_c(S')$ in the constriction, an oscillatory behavior of $I_c(B)$ emerges, as exhibited by samples C and D [see Fig. 5(a)]. The corresponding measurements were taken at temperatures below the T_c's of the weak links, *i.e.* at 4 K and 2.5 K, respectively.

Although the observed oscillations resemble the Fraunhofer patterns in SNS Josephson junctions described by $I_c(B) = I_0|\mathrm{sinc}(\alpha B)|$, with sinc the cardinal function, $\alpha = \pi LW/\Phi_0$, Φ_0 the flux quantum, and L and W the length and the width of the normal region, any fitting attempt using this expression leads to poor agreement with the experimental data. This is not surprising considering that the weak link generated by EA largely exceeds, both in length and width, the superconducting coherence length. In this limit, the physical mechanism giving rise to the observed oscillations of critical current necessarily involves Abrikosov vortices[33] and therefore the current-phase relation no longer follows a sinusoidal dependence.[34] Furthermore, unlike SIS Josephson junctions, the oscillation period in our $I_c(B)$ does not seem to necessarily correspond to one flux quantum in the weak-link area. To shed light on what is exactly occurring in the samples, we recall the TDGL simulations, parametrized according to the excellent fit of $R(T)$ characteristics in Fig. 3(b). The results are shown in Fig. 5(b), and demonstrate a good quantitative agreement to experimental data for the $I_c(0)$ of samples C and D, scaled to the $I_c(0)$ of the virgin sample, taken at the same respective temperatures as in the experiment (the nominal values of calculated $I_c(0)$ for all samples were within 10% discrepancy from the experimentally measured ones). Moreover, the oscillatory nature of $I_c(B)$ characteristics is also captured, fully in line with the vortex nucleation and dynamics behavior described in Fig. 4. This is illustrated by the Cooper-pair density maps shown in the insets of Fig. 5(b), where a phase-slip is seen at the onset of dynamics at zeroth oscillation, one crossing vortex at the first oscillation, and two crossing vortices at the second oscillation of $I_c(B)$. Finally, the matching of the maxima in $I_c(B)$ for the two samples in theory and experiment, as well as the correlation between the detected periods of oscillations, are all in good agreement with the experimental curves. We note that the simulations verify the difference of the oscillation period between samples C and D observed in Fig. 5(a), without invoking modifications of the weak-link area (*i.e.* the parameter b is the same for both samples). This confirms the premise that the oscillation period does not exactly correspond to one flux quantum in the weak-link area, as one may naively assume, but instead all parameters play a role in the resulting $I_c(B)$ characteristic of the sample. As one difference between the theory and experiment we note the much stronger barrier for vortex entry in simulations when the sample is in the Meissner state, in spite of the nearly ideal copied geometry of the sample from the experiment. This can be attributed to the fine damages to the sample edges during lithography, or local variations in the superconducting properties at the borders that are not taken into account in the simulations.

As a final check, we explored the magnetoresistance oscillations in the dissipative regime. Namely, we measured the magnetoresistance of sample C at a fixed transport current of 1 μA, and revealed clear oscillations in the temperature range between 4 K and 5 K, as shown in Fig. 5(c). As expected, every maximum of dissipation corresponds well with a minimum in critical current. Interestingly, no temperature dependence of the position of these maxima is observed. To corroborate the experimental measurements, we also calculated the magnetoresistance oscillations for sample C, using the same parametrization as in Fig. 5(b) and same applied current as for the calculations of Fig. 3(b), for temperature varied between 4 and 5 K. As plotted in Fig. 5(d), we confirm the excellent agreement with experimental findings, as the position of maxima in magnetoresistance ideally correspond to the minima of $I_c(B)$ characteristics, and exhibit no temperature dependence close to the critical temperature of the weak link. In other words, we observe that the position of the minima in $I_c(B)$ no longer changes once the resistive state in the weak link is reached. At lower temperatures however, where the superconducting state of the weak link is restored, the minima of the $I_c(B)$ characteristics shift to higher applied fields. This is again consistent with our initial picture in Fig. 4, linking the tunable $I_c(B)$ characteristics of our samples to the tunable conditions for additional vortex crossings in the weak link, and not to magnetic interference patterns leading to Josephson vortices in SNS junctions.[29,35] Note that other than the fundamental peaks observed in Fig. 5(c), there are additional fine structure features whose origin remains to be determined.

3 Conclusion

In summary, we demonstrated the fabrication and *in situ* fine tuning of a superconducting weak link, using electro-annealing (EA) on Nb nanoconstrictions. We show that the EA process can be useful in a two-fold manner: either to improve the superconducting properties in the targeted area for weak annealing currents, or to suppress the superconducting properties *via* amorphization of the material by larger applied currents. In cases where a clear weak link is formed in the nanoconstriction between the superconducting banks we measured Fraunhofer-like oscillations in the critical current as a function of the magnetic field and demonstrated that such characteristic is tunable in a broad range by successive electro-annealing processes. We have proven the controllability of the procedure by direct comparison to numerical simulations of the outcome, nearly fully parametrized from experimental considerations and observations. We conclude that our method indeed delivers the fabrication and control of weak links at nanoscale, tunable *in situ*, thus beyond the available state-of-the-art where weak links are either preformed and not tunable, or dependent on a rather involved and less practical setup.

4 Methods

4.1 Experimental details

The investigated samples consist of 50 nm-thick Nb films deposited by electron beam evaporation onto a Si substrate terminated with a 100 nm-thick SiO_2 layer under UHV and subsequently capped with 5 nm of Si for protection.[21] The lithographic electron exposure has been carried out in a Nanobeam nB5 platform with an electron beam energy of 80 keV. Afterwards, an Al mask is fabricated by e-beam evaporation, followed by a lift-off. To remove the Nb not covered by the Al, we performed reactive ion etching using SF_6 during 10 s. Finally, the Al is removed using the base developer MF-26A. A scanning electron microscopy (SEM) image of the lithographically defined 130 nm wide constriction is shown in Fig. 1(a). The voltage contacts are symmetrically placed at about 1 μm away from the central constriction.

For all electric transport measurements presented in this work, the electro-annealing has been carried out in a cryogenic environment with bath temperature $T_B \sim 10$ K above the critical temperature of the Nb film (~8.88 K). The electro-annealing process is achieved by software control with a feedback loop as described in ref. 22. It basically consists in the application of a voltage ramp to attain a constant conductance rate of $-2G_0$ s^{-1}, where G_0 is the quantum of conductance, while simultaneously monitoring the consequent resistance change. The whole control algorithm is stopped within 5 seconds once a certain maximum current, so called the electro-annealing current I_{EA}, is achieved. The software controlled feedback loop allows reacting upon abrupt resistance jumps and ensures a progressive evolution of the sample's resistance in time. Both, the electrical transport measurements and electro-annealing processes were carried out in a modified commercial Quantum Design-PPMS cryostat equipped with a 9 T magnet. The sample is mounted in a sealed chamber providing a temperature stability better than 1 mK in a He gas atmosphere (20 mbar).

4.2 Details of numerical simulations

In the theoretical segment of this work we use the dimensionless time-dependent Ginzburg–Landau model, capable of providing the information about evolution of the inhomogeneous superconducting condensate in the presence of external potentials (namely, magnetic vector potential **A** and electrostatic potential φ). The governing equations of the model are

$$u\left(\frac{\partial}{\partial t}+\mathrm{i}\varphi\right)\Delta = \left[p(\mathbf{r})f(T)-\frac{g(T)}{p(\mathbf{r})}|\Delta|^2\right]\Delta + z(\mathbf{r})(\nabla-\mathrm{i}\mathbf{A})^2\Delta, \quad (2)$$

$$\nabla[z(\mathbf{r})\nabla\varphi] = \nabla J_s = \nabla\left[\frac{z(\mathbf{r})}{p(\mathbf{r})}|\Delta|^2(\nabla\theta-\mathbf{A})\right], \quad (3)$$

where time is measured in units of $\tau_{GL}(0) = \pi\hbar/8uk_BT_c^{(0)}$, corresponding to the Ginzburg–Landau relaxation time of the order parameter, $\Delta = |\Delta|e^{i\theta}$, at 0 K (where k_B is the Boltzmann's constant, $\hbar$ is the reduced Planck's constant, $T_c^{(0)}$ is the critical temperature of the virgin sample, and microscopic parameter $u = 5.79$ corresponds to the ratio of the relaxation times for the order parameter magnitude, $|\Delta|$, and its phase, θ), while all distances are expressed in units of coherence length, $\xi(0) = \sqrt{\pi\hbar D^{(0)}/8k_BT_c^{(0)}}$, also at 0 K (where $D^{(0)}$ is the diffusion parameter of the virgin sample). Order parameter is scaled with its bulk value at 0 K, $\Delta_{GL}(0) = 4\sqrt{u}k_BT_c^{(0)}/\pi$. Unit of electrostatic potential is $\varphi_{GL}(0) = \hbar/e^*\tau_{GL}(0)$ (e^* is the charge of the Cooper pair), and vector potential is scaled by $Q_{GL}(0) = H_{c2}(0)\xi(0)$, where $H_{c2}(0) = \hbar/e^*\xi(0)^2$ is the bulk upper critical field, also used as a unit for magnetic field. In these units, current density is given in $J_{GL}(0) = \sigma^{(0)}\varphi_{GL}(0)/\xi(0)$, where $\sigma^{(0)} = e^{*2}N(0)D^{(0)}/2$ is the normal-state conductance of the virgin sample ($N(0)$ is the density of states).

The inhomogeneity of the material properties due to electro-annealing, such as critical temperature, T_c, mean free path, ℓ, and normal-state conductance, σ, is accounted for through spatially-dependent kernels $p(\boldsymbol{r})$ and $z(\boldsymbol{r})$. Inside the weak link, variation of the critical temperature is described *via* $p(\boldsymbol{r}) = T_c(\boldsymbol{r})/T_c^{(0)}$, while everywhere outside the weak link $p(\boldsymbol{r}) = 1$. From the microscopic derivation of TDGL theory[36] one knows that in the dirty limit diffusion parameter is linearly dependent on the mean free path ($D \propto \ell$), and since we have already established that $\ell \propto \sigma = 1/\rho$, one can use a unique function $z(\boldsymbol{r})$ to simultaneously describe spatial variations of both mean free path and normal-state conductance. In our model, $z(\boldsymbol{r}) = \rho_{WL}/\rho_0$ in the weak link region, and $z(\boldsymbol{r}) = 1$ outside.

In order to extend the applicability of TDGL model to a broader temperature range, we introduce thermal kernels $f(T) = \left[1-\frac{T^2}{T_c(\mathbf{r})^2}\right]\Big/\left[1+\frac{T^2}{T_c(\mathbf{r})^2}\right]$ and $g(T) = \left[1+\frac{T^2}{T_c(\mathbf{r})^2}\right]^{-2}$ as readily documented in literature to provide excellent agreement of the GL model with experiments on mesoscopic superconductors.[27,37] At the superconductor–vacuum (SV) interface, neither supercurrent nor normal current flows perpendicularly to the interface, $\boldsymbol{n}_{SV}(\nabla - i\mathbf{A})\Delta = 0$, and $\boldsymbol{n}_{SV}\nabla\varphi = 0$ ($\boldsymbol{n}_{SV}$ is the unit vector perpendicular to the SV boundary). Applied current density J_a is introduced at normal contacts-superconductor boundary (NS), where $\boldsymbol{n}_{NS}\nabla\varphi = J_a$, and $\Delta = 0$ ($\boldsymbol{n}_{NS}$ is the unit vector perpendicular to the NS interface).

Finally, the sample length was 1600 nm and faithfully respecting the geometry of the constriction taken directly from the experimental SEM image with grid resolution of 1 nm × 1 nm. The material parameters of the weak link adopted from the experimental data for sample C were $\rho_{WL} = 20.4$ μΩ cm and corresponding mean free path $\ell_{WL} = 1.83$ nm, with either homogeneous critical temperature $T_c^{WL} = 5.46$ K of the weak link, or the inhomogeneous distribution of T_c in the weak link, with $T_c|_{x=0} = 4.49$ K in the center. In the case of sample D, the material parameters were $\rho_{WL} = 24.1$ μΩ cm (with $\ell_{WL} = 1.55$ nm), $T_c^{WL} = 3.51$ K in the homogeneous weak link, and $T_c|_{x=0} = 2.82$ K in the inhomogeneous weak link. Bath temperatures for samples C and D were taken to be the same as in experiment, thus 4 K and 2.5 K, respectively.

4.2.1 Depairing current. In order to derive the expression for the temperature dependence of the depairing current $J_{DP}(T)$, one needs to start from the supercurrent density $J_s(T)$ expressed in real units, obtained from time-dependent Ginzburg–Landau framework as:

$$J_s = \frac{N(0)\pi e^* D}{4k_B} T_c \frac{{\Delta_{GL}}^2(T)}{\xi(T)} |\Delta|^2 (\nabla\theta - \mathbf{A}). \quad (4)$$

Within the TDGL model expanded to work in a broader temperature range, the bulk value of the order parameter at a given temperature T is given as $\Delta_{GL}(T) = \Delta_{GL}(0)\sqrt{f(T)/g(T)}$, while the coherence length is $\xi(T) = \xi(0)/\sqrt{f(T)}$. Since the term $|\Delta|^2(\nabla\theta - \mathbf{A})$ corresponds to the dimensionless supercurrent density, the remaining parameters on the right-hand side of eqn (4) constitute the quantity used to scale supercurrent density at a given temperature, $J_{GL}(T)$. It is well known from the literature[38] that depairing current density can be related to $J_{GL}(T)$ as $J_{DP}(T) = \frac{2}{3\sqrt{3}} J_{GL}(T) \approx 0.385 J_{GL}(T)$. From there, it is possible to obtain the full expression for the depairing current as a function of temperature as

$$J_{DP}(T) = 0.385 \frac{8\sqrt{2} u e^* N(0) {k_B}^{3/2}}{\pi^{3/2}\sqrt{\hbar}} {T_c}^{3/2} \sqrt{D} \frac{f^{3/2}}{g}. \quad (5)$$

By explicitly including the thermal dependence of functions $f(T)$ and $g(T)$ into eqn (5), and from the fact that $D \sim \ell$, one finally obtains:

$$J_{DP}(T) = C {T_c}^{3/2} \sqrt{\ell} \left(1 - \frac{T^2}{{T_c}^2}\right) \sqrt{1 - \frac{T^4}{{T_c}^4}}, \quad (6)$$

where $C = 4.355 u e^* N(0) {k_B}^{3/2} \sqrt{v_F}/\pi^{3/2}\sqrt{\hbar}$.

Conflicts of interest

The authors declare no conflicts of interest.

Acknowledgements

The authors thank the Fonds de la Recherche Scientifique – FNRS, the ARC grant 13/18-08 for Concerted Research Actions, financed by the French Community of Belgium (Wallonia-Brussels Federation), the Research Foundation – Flanders (FWO-Vlaanderen) and the COST action NanoCoHybri (CA16218). The work is also suppported by Methusalem Funding by the Flemish Government. J. Lombardo acknowledges support from F. R. S.-FNRS (FRIA Research Fellowship). The LANEF framework (ANR-10-LABX-51-01) and the Nanoscience Foundation are acknowledged for their support with mutualized infrastructure. The work of A. V. Silhanek is partially supported by PDR T.0106.16 of the F. R. S.-FNRS. The authors thank the ULg Microscopy facility CAREM for part of the SEM investigations.

References

1 B. D. Josephson, *Phys. Lett.*, 1962, **1**, 251–253.
2 D. Cohen, *Science*, 1972, **175**, 664–666.
3 C. A. Hamilton and Y. H. Tang, *Metrologia*, 1999, **36**, 53.
4 C. A. Hamilton, *Rev. Sci. Instrum.*, 2000, **71**, 3611–3623.
5 M. A. Nielsen and I. L. Chuang, *Quantum Computation and Quantum Information*, Cambridge University Press, 2000.
6 Y. Makhlin, G. Schön and A. Shnirman, *Rev. Mod. Phys.*, 2001, **73**, 357–400.
7 D. Halbertal, J. Cuppens, M. B. Shalom, L. Embon, N. Shadmi, Y. Anahory, H. Naren, J. Sarkar, A. Uri, Y. Ronen, *et al.*, *Nature*, 2016, **539**, 407–410.
8 R. Gross, P. Chaudhari, D. Dimos, A. Gupta and G. Koren, *Phys. Rev. Lett.*, 1990, **64**, 228–231.
9 L. Angers, F. Chiodi, G. Montambaux, M. Ferrier, S. Guéron, H. Bouchiat and J. C. Cuevas, *Phys. Rev. B: Condens. Matter Mater. Phys.*, 2008, **77**, 165408.
10 O. Vavra, W. Pfaff and C. Strunk, *Appl. Phys. Lett.*, 2009, **95**, 062501.
11 A. Sivakov, A. Glukhov, A. Omelyanchouk, Y. Koval, P. Müller and A. Ustinov, *Phys. Rev. Lett.*, 2003, **91**, 267001.
12 M. Amado, A. Fornieri, F. Carillo, G. Biasiol, L. Sorba, V. Pellegrini and F. Giazotto, *Phys. Rev. B: Condens. Matter Mater. Phys.*, 2013, **87**, 134506.
13 O. Vavra, W. Pfaff, R. Monaco, M. Aprili and C. Strunk, *Appl. Phys. Lett.*, 2013, **102**, 072602.
14 L. Bégon-Lours, V. Rouco, A. Sander, J. Trastoy, R. Bernard, E. Jacquet, K. Bouzehouane, S. Fusil, V. Garcia, A. Barthélémy, M. Bibes, J. Santamaría and J. E. Villegas, *Phys. Rev. Appl.*, 2017, **7**, 064015.
15 A. K. Misra, *Metall. Trans. A*, 1985, **16**, 1354–1355.
16 A. K. Misra, *Metall. Trans. A*, 1986, **17**, 358–360.
17 R. Takemoto and H. Mizubayashi, *Acta Metall. Mater.*, 1995, **43**, 1495–1504.
18 H. Mizubayashi and S. Okuda, *Phys. Rev. B: Condens. Matter Mater. Phys.*, 1989, **40**, 8057.
19 T. Aref and A. Bezryadin, *Nanotechnology*, 2011, **22**, 395302.
20 B. Moeckly, R. Buhrman and P. Sulewski, *Appl. Phys. Lett.*, 1994, **64**, 1427.
21 X. D. A. Baumans, J. Lombardo, J. Brisbois, G. Shaw, V. S. Zharinov, G. He, H. Yu, J. Yuan, B. Zhu, K. Jin, R. B. G. Kramer, J. V. de Vondel and A. V. Silhanek, *Small*, 2017, **13**, 1700384.
22 X. D. A. Baumans, D. Cerbu, O. Adami, V. S. Zharinov, N. Verellen, G. Papari, J. E. Scheerder, G. Zhang, V. V. Moshchalkov and A. V. Silhanek, *Nat. Commun.*, 2016, **7**, 10560.
23 W. DeSorbo, *Phys. Rev.*, 1963, **132**, 107.
24 J. Halbritter, *App. Phys. A*, 1987, **43**, 1–28.
25 Y. Monfort, D. Bloyet, J. Villégier and D. Duret, *IEEE Trans. Magn.*, 1985, **21**, 866.

26 C. Delacour, L. Ortega, M. Faucher, T. Crozes, T. Fournier, B. Pannetier and V. Bouchiat, *Phys. Rev. B: Condens. Matter Mater. Phys.*, 2011, **83**, 144504.
27 G. Stenuit, S. Michotte, J. Govearts and L. Piraux, *Supercond. Sci. Technol.*, 2005, **18**, 174.
28 F. S. Bergeret and J. C. Cuevas, *J. Low Temp. Phys.*, 2008, **153**, 304.
29 J. C. Cuevas and F. S. Bergeret, *Phys. Rev. Lett.*, 2007, **99**, 217002.
30 G. R. Berdiyorov, M. V. Milošević, M. L. Latimer, Z. L. Xiao, W. K. Kwok and F. M. Peeters, *Phys. Rev. Lett.*, 2012, **109**, 057004.
31 D. Y. Vodolazov, *Phys. Rev. B: Condens. Matter Mater. Phys.*, 2013, **88**, 014525.
32 L. Embon, Y. Anahory, Z. L. Jelić, E. O. Lachman, Y. Myasoedov, M. E. Huber, G. P. Mikitik, A. V. Silhanek, M. V. Milošević, A. Gurevich and E. Zeldov, *Nat. Commun.*, 2017, **8**, 85.
33 K. K. Likharev, *Rev. Mod. Phys.*, 1979, **51**, 101.
34 K. Hasselbach, D. Mailly and J. R. Kirtley, *J. Appl. Phys.*, 2002, **91**, 4432.
35 D. Roditchev, C. Brun, L. Serrier-Garcia, J. C. Cuevas, V. H. L. Bessa, M. V. Milošević, F. Debontridder, V. Stolyarov and T. Cren, *Nat. Phys.*, 2015, **11**, 332.
36 R. J. Watts-Tobin, Y. Krähenbühl and L. Kramer, *J. Low Temp. Phys.*, 1981, **42**, 459.
37 A. Müller, M. V. Milošević, S. E. C. Dale, M. A. Engbarth and S. J. Bending, *Phys. Rev. Lett.*, 2012, **109**, 197003.
38 M. Tinkham, *Introduction to Superconductivity*, Dover Publications, 2004.

